Icarus 373 (2022) 114774

Contents lists available at ScienceDirect

Icarus

journal homepage: www.elsevier.com/locate/icarus

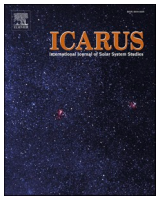

Evaluating the role of volatiles in bedrock chute formation on the moon and mars

Janette N. Levin [a,b,*], James L. Dickson [a], Michael P. Lamb [a]

[a] Division of Geological & Planetary Sciences, California Institute of Technology, Pasadena, CA, USA
[b] Department of Earth, Environmental, and Planetary Sciences, Brown University, Providence, RI, USA

A B S T R A C T

Steep channel-like landforms—referred to here as bedrock chutes—line the rocky walls of some craters on the Moon and Mars. The role of volatiles, such as H_2O or CO_2, or dry rockfall in the formation of bedrock chutes is unknown on either planetary body. To test whether bedrock chute formation on Mars involved volatile activity, we used digital elevation models of Mars generated from HiRISE and CTX stereo-imagery to survey 4–9 km diameter craters globally and measure chute morphology as a function of latitude and orientation—properties that might co-vary with volatile activity. We also analyzed bedrock chutes on the Moon, which is presumably devoid of significant erosion due to volatile activity, using LROC NAC data, to serve as a volatile-free endmember for comparison with Mars. Martian bedrock chutes occur at all latitudes and have median values of chute spacing (wavelength) of ~300 m, relief of ~15 m, and slope of ~33°. Chutes on the Moon are less common and are generally steeper (~41°) with less relief (~5 m) as compared to Mars. While dry rockfall might have formed bedrock chutes on both the Moon and Mars, martian chutes are systematically deeper on pole-facing slopes between 10°S- 30°S indicating a likely role for volatile activity in chute formation. Bedrock chutes are also deeper where they co-occur with well-incised martian gully channels. The latitude-dependence for deeper bedrock chutes on pole-facing slopes extends to lower latitudes than gullies—within the contemporary tropics—indicating the potential for volatile-related activity closer to the equator than documented for gullies or other ice-related features on Mars. Chutes carved into bedrock likely form slowly compared to gully channels, which are incised into more erodible ice-cemented sediment, and therefore might provide a longer record of environmental conditions over larger swaths of Mars.

1. Introduction

Impact craters are abundant on Mars and the Moon. They degrade over time, which yields important information about the rates of weathering and erosion processes (Craddock and Howard, 2000; Golombek et al., 2014). Most modeling studies assume that crater degradation can be described by topographic diffusion due to soil creep from repetitive disturbance events such as micro-impacts (Armitage et al., 2011; Fassett and Thomson, 2014; Golombek et al., 2014; Sweeney et al., 2018). In contrast to fluvial erosion that tends to incise channels and valleys, topographic diffusion smooths the topography and relaxes crater wall slopes over time (Howard, 2007). For instance, the degree of crater wall dissection on Mars is used as an indicator of the relative amount of fluvial activity vs soil creep (e.g., Hughes et al., 2019). However, many crater walls on the Moon and Mars are dissected by linear, steep, channel-like landforms, referred to herein as bedrock chutes (Fig. 1), with an unknown origin.

Recent work has suggested that bedrock chutes can form entirely due to dry rockfall (Beer et al., 2020; Kumar et al., 2013; Sun et al., 2021). However, modeling studies that typically consider only fluvial incision and soil creep (Howard, 2007) are not equipped to address the role of dry rockfall in chute formation. Bedrock chutes are observed on Earth—for example in Meteor Crater, Arizona (Kumar et al., 2010), and in alpine landscapes—but due to the ubiquity of liquid water on Earth, it is difficult to isolate the roles of dry rockfall and rock avalanches from runoff, debris flow, or snow avalanches and ice in chute formation (Montgomery and Korup, 2011; Sanders et al., 2014). Consequently, we currently lack an understanding of how bedrock chutes form, whether H_2O or CO_2 are necessary for their formation, or whether they can be carved by entirely dry rockfall.

On Mars, bedrock chutes are observed primarily on fresh crater rims at all latitudes, with varying morphologies (Dickson and Head, 2009). These landforms tend to occur in the steeply sloping rocky zone of craters just below the crater rim. Some craters have small, narrow chutes (Fig. 1b), while in other cases chutes coalesce into large bedrock alcoves (Fig. 1c,d). Bedrock chutes are distinct from, but in some cases related to, the more extensively studied martian gullies (Malin and Edgett, 2000; Harrison et al., 2015). Most commonly observed in the 30° - 60° latitude band in either hemisphere, martian gullies, with the exception of those found on dunes (Diniega et al., 2010), are comprised of a main

* Corresponding author at: Department of Earth, Environmental, and Planetary Sciences, Brown University, Providence, RI, USA
E-mail address: janette_levin@brown.edu (J.N. Levin).

https://doi.org/10.1016/j.icarus.2021.114774
Received 26 March 2021; Received in revised form 20 October 2021; Accepted 28 October 2021
Available online 30 October 2021

channel, a depositional fan, and an alcove (Malin and Edgett, 2000) (Fig. 1d). In some cases, gully alcoves contain coalescing bedrock chutes that make up the channelized skeleton of the alcove (Fig. 1d). Unlike gully channels and fans, which typically form within regolith ("pasted-on terrain") (Christensen, 2003) that undergoes removal during interglacial periods like the present (Head et al., 2003) or within loose dune material (Diniega et al., 2010), bedrock chutes are not as easily removed over time because they are carved into rock. Though some recent (~5–10 Ma) modification of bedrock spurs in crater rims by small scale glaciers has been documented (Conway et al., 2018), bedrock chutes are far less transient than gully channels, which have been shown to cross-cut previous gullies, incise older fans and be removed entirely over time (Dickson et al., 2015). Thus, understanding the formation of bedrock chutes, and whether it requires volatile activity, is important because these landforms might hold information from climates dating back to the formation of the host crater, not just the most recent climate recorded in gully channels.

Gullies are Late Amazonian landforms that have been the subject of detailed study since their discovery (Malin and Edgett, 2000) due to their resemblance to fluvial or debris flow channels and fans on Earth (Costard et al., 2002). Gullies are among the youngest geological features on Mars, with superposed crater populations and stratigraphic relationships indicating that their formation was within the last few million years (e.g., Reiss et al., 2004; Schon et al., 2009). Gully formation has been proposed to involve seeping groundwater (Malin and Edgett, 2000), snow melt (Christensen, 2003; Costard et al., 2002; Dickson et al., 2007, e.g.) or seasonal CO_2 defrosting activity (Dundas et al., 2015; Dundas et al., 2012; Pilorget and Forget, 2016). Volatile activity is supported by the spatial occurrence of gullies. Classic, hundred-meter scale martian gullies (Malin and Edgett, 2000) are located mostly between 30°-60° latitude in each hemisphere, with some higher-latitude observations (Balme et al., 2006; Dickson et al., 2007; Harrison et al., 2015; Heldmann and Mellon, 2004; Kneissl et al., 2010; Malin and Edgett, 2000; Milliken et al., 2003), and display a strong orientation preference for colder, pole-facing slopes in the lower mid-latitude of either hemisphere (30°-45°) (Dickson et al., 2007; Heldmann and Mellon, 2004). Strong orientation preferences for gullies were first documented using Mars Orbiter Camera (MOC) data (Heldmann and Mellon, 2004), and have since been confirmed and refined using greater coverage from Mars Reconnaissance Orbiter (MRO) data (Conway et al., 2019a). These distribution patterns suggest volatile-influenced processes in their formation, as gullies are dominantly

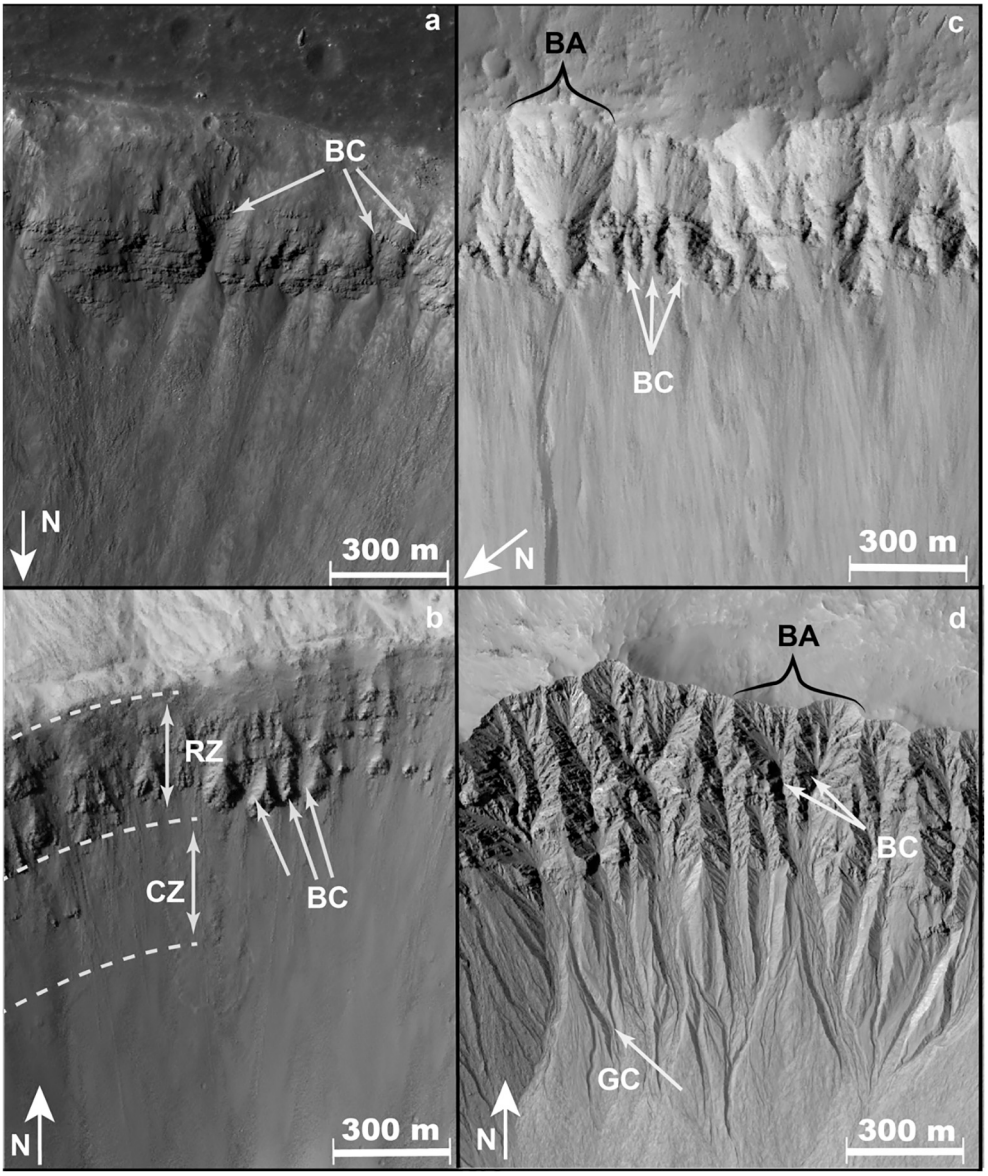

Fig. 1. Bedrock chutes (BC) are observed on a) steep slopes on the Moon (Image: LRO NAC M190423336L GSFC/ASU/MSSS). They are also found at all latitudes on Mars. We classified the area between the crater rim and the end of visible bedrock as the rocky zone (RZ), and the area of equal thickness directly below the bedrock as the colluvial zone (CZ). Martian bedrock chutes have varying amounts of incision, such as b) small, regular and shallow chutes (HiRISE ESP_036512_1870 6°N 94°E NASA/JPL-Caltech/UoA) c) several chutes coalescing into a bedrock alcove (BA) (Image: HiRISE PSP_004151_1810 1°N 161°E NASA/JPL-Caltech/UoA) and d) well incised, branching alcoves with gully channels (GC) emanating down into the colluvial zone below them (38°S -167°E Image: HiRISE ESP_048693_1420 NASA/JPL-Caltech/UoA).

found where CO_2 and H_2O ice can accumulate on Amazonian Mars (Hecht, 2002) and where steep slopes are available (Conway et al., 2019b; Dickson et al., 2007).

Given that gully channels and bedrock chutes are both channel-like landforms on crater walls, and that chutes in some cases are part of gully alcoves, then it is reasonable to ask whether bedrock chutes also require volatile activity to form. However, bedrock chutes are not present upslope from all well-incised gully channels, and, unlike gullies, bedrock chutes are observed at all latitudes (Dickson and Head, 2009). Bedrock may be able to hold its shape and create a topographic feedback that results in channelization entirely through dry rockfall on steep slopes, leading to a chute (Beer et al., 2020; Sun et al., 2021). Support for this hypothesis comes from the Moon where bedrock chutes are observed (Fig. 1a) and where erosion due to volatile activity is unlikely (Bart, 2007; Kokelaar et al., 2017; Kumar et al., 2013). Thus, it seems possible that bedrock chutes could form by dry rockfall without the aid of H_2O or CO_2, even on Mars.

While the properties and distributions of martian gullies have been studied extensively (Conway et al., 2019a; Dickson et al., 2015; Harrison et al., 2015; Mangold et al., 2010), bedrock chutes have not been studied in three dimensions at the global scale. To understand the extent to which volatiles were involved in carving bedrock chutes on Mars, we used high-resolution stereo imagery to globally survey bedrock chutes and to measure their wavelength, relief, and topographic slope. We performed similar analyses of bedrock chutes on the Moon, which we treated as a control environment for chutes formed through entirely dry processes. Given the strong ties between gully activity and seasonal frost locations, we considered the co-occurrence of well-incised gully channels on the same crater wall as bedrock chutes as a likely indicator of volatile influence. Along that same line of reasoning, we compared bedrock chute attributes as a function of latitude and orientation dependence as potential indicators of volatile influence.

2. Methods

In order to systematically study trends in the morphologies of bedrock chutes on a global scale on the Moon and Mars, we extracted measurements of chute wavelength, chute relief, and chute topographic slope for chutes found along crater rims from stereo-photogrammetric data generated using Ames Stereo Pipeline (Beyer et al., 2018). For Mars, we used a global database of craters >1 km in diameter (Robbins and Hynek, 2012) to survey and locate fresh impact craters with intact rims and visible signs of bedrock (Section 2.1). We developed and applied an automated rim mapping tool (Section 2.2) to Context Camera (CTX) (Malin et al., 2007) digital elevation models (DEMs) to generate topographic profiles and analyzed them to measure characteristic wavelength, chute relief, and slope of north and south-facing walls of each crater (Section 2.3). We both extracted profiles manually and used the automated rim mapping tool to generate topographic profiles from several High Resolution Imaging Science Experiment (HiRISE) (McEwen et al., 2007) DEMs and compared the results to check the consistency of our CTX measurements (Section 2.4). As a basis of comparison for the martian chutes, we made identical manual measurements of bedrock chutes on the Moon from LROC NAC (Lunar Reconnaissance Orbiter Camera - Narrow Angle Camera) DEMs (Section 2.5).

Uncertainty in pointing of HiRISE, CTX and LROC can introduce errors in topographic measurements due to slightly inaccurate placement of the desired stereo target on its respective coordinate frame. To account for this, we aligned HiRISE and CTX DEMs to underlying MOLA data (see Supplementary Materials). The precision of LROC images on the Moon is unknown at the global scale, so we did not align LROC DEMs with global topography. The errors due to this uncertainty are not expected to bias measurements systematically and should be distributed randomly through our data. The lack of independent high-resolution topography prevents us from providing a more precise measurement of error.

2.1. Mars survey

Martian bedrock chutes are typically tens to hundreds of meters in width, and thus require targeted stereo topography to sufficiently resolve their three-dimensional morphology. We used CTX to broadly survey bedrock chutes on the global scale, due to its greater surface coverage. HiRISE was used to verify CTX measurements and for detailed analyses of specific features.

We analyzed bedrock chutes that form along the inner rim of fresh impact craters. We used a global database of craters >1 km in diameter (Robbins and Hynek, 2012) to select all mapped craters that have diameters between 4 and 9 km and rim to floor elevation changes that exceed 400 m. These criteria were chosen to target fresh, steep-walled craters with minimal infilling that would be small enough to consistently fit into a CTX swath. We isolated all such craters that intersected a distribution map of 20 m/px CTX DEMs derived using Ames Stereo Pipeline (ASP) (Beyer et al., 2018), totaling 2876 craters (Fig. 2b). As overlapping CTX image pairs were not necessarily targeted for stereo topography with optimal emission and solar incidence geometries, DEMs were inspected by eye for completeness of coverage and assessment of quality, resulting in 441 craters with high-quality CTX DEM coverage. Of these 441 craters, we selected those that had some visible bedrock morphology (i.e., visible layering or blocky texture) along the inner rim and those that adequately passed through our automated crater rim mapping tool (Section 2.2) and subsequent filtering (Section 2.3) as described below. After filtering, the final crater count was 243 (blue dots in Fig. 2b), which are distributed across ranges of latitude, elevation and host geological units (Tanaka et al., 2014).

We also noted the presence of gully channels emanating downslope from bedrock chutes (Fig. 1d), focusing on the well-incised, sinuous, mid-latitude gullies as mapped by Harrison et al. (2015), using the alcove/channel/fan definition for gullies (Malin and Edgett, 2000). Harrison et al. (2015) excluded small, linear, shallowly incised troughs on talus slopes near the equator (Auld and Dixon, 2016) because these have different properties (e.g., sinuosity (Mangold et al., 2010) and depth-of-incision (Dickson et al., 2015)) as compared to mid-latitude gully channels.

2.2. Automated crater rim mapping

Exposed bedrock chutes are consistently observed on steep slopes along the inner rim crest of impact craters. To systematically measure bedrock chutes, we developed an algorithm to estimate the location of a crater rim crest using slope measurements. This tool takes as input (1) a CTX DEM that covers the entire crater and (2) a circle inscribed within the crater. The slope of each pixel inside the circle is then calculated using a third-order finite difference method (Horn, 1981) from the Slope tool in the ArcGIS Python module, *arcpy*. In fresh craters with an intact rim, the steepest slopes are found near the crest of the crater rim. The algorithm locates continuous pixels with slope values 27°- 60° and uses them to generate a polygon estimating the shape of the crater (see Supplementary Materials). This polygon is then contracted by 25-m increments to generate parallel, concentric profiles downslope from the crater rim (Fig. 3a), which we used to make measurements of chute wavelength and relief (Section 2.3).

Our tool worked best on fresh craters with intact rims, provided calculations were performed on input DEMs of reasonable quality. Stereo photogrammetry produced null values in heavily shadowed locations, and struggled to find correlation on very smooth surfaces, so the algorithm produced unavoidably erroneous rim locations on heavily shadowed or very smooth slopes. Other possible errors occurred in areas of heavily degraded or mantled crater rims, where the slope is consistently <27°, and in craters with sharply raised rims, where there are large areas of high sloping terrain directly on the outer perimeter of the rim. Various filters were implemented into further analysis to account for polygonization errors (Section 2.3).

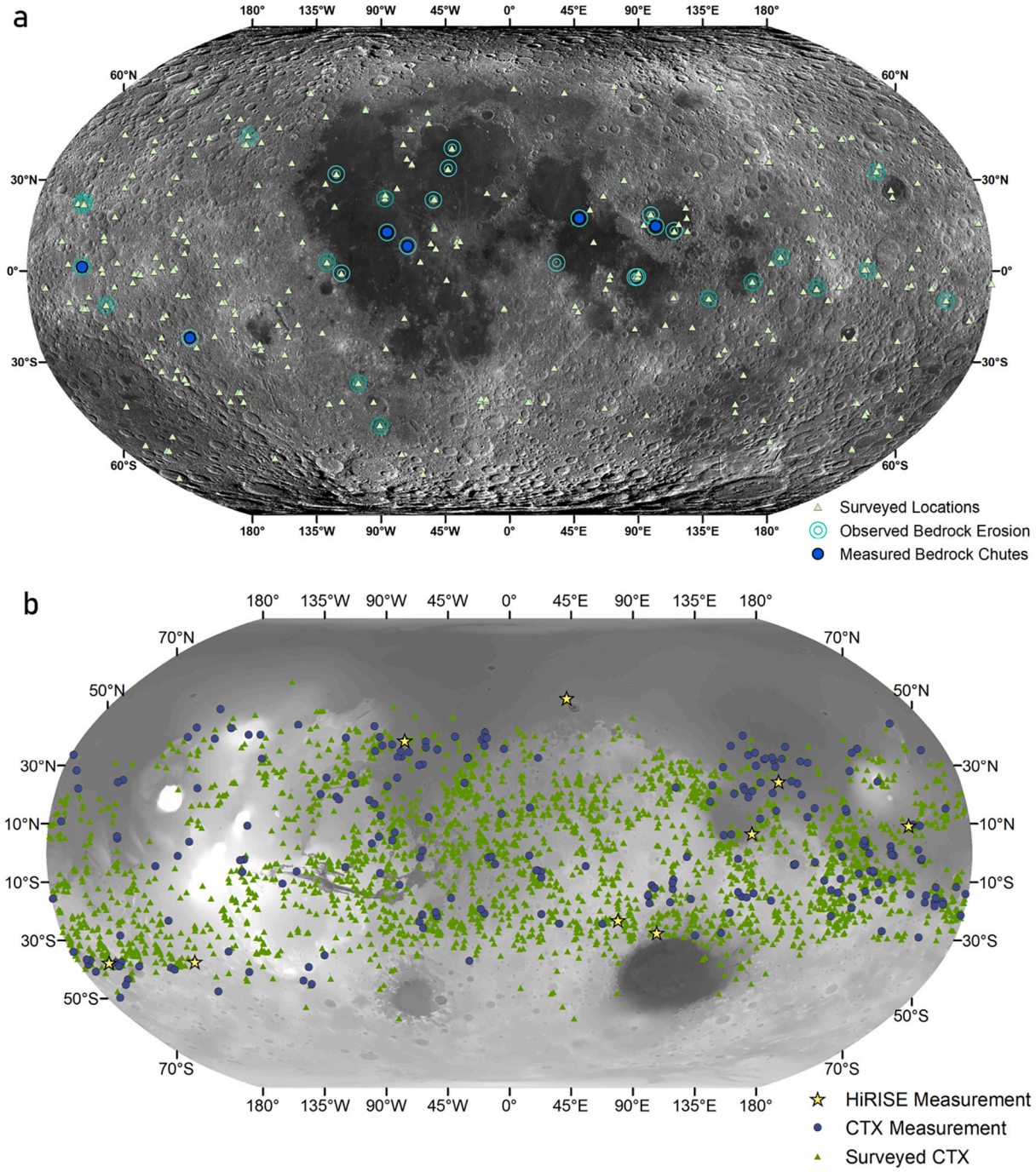

Fig. 2. a) We surveyed 403 lunar craters and noted all locations with visible bedrock erosion. DEMs were generated where possible and measurements of chute relief were made on 6 DEMs. (WAC Mosaic GSFC/ASU/MSSS). b) We surveyed 2876 martian craters for completeness of DEM coverage and bedrock erosion and made CTX measurements of bedrock chute relief of 243 craters. We measured 9 craters with HiRISE DEMs. (MOLA (Smith et al., 2001)).

2.3. Bedrock chute measurements using CTX

Parallel, concentric profiles extracted from our automated crater rim mapping (Section 2.2) were used to quantitatively characterize the morphology of bedrock chutes on crater walls using CTX data with a spatial resolution of ~20 m/px (Malin et al., 2007). We extracted topography measurements from the DEM along each profile within the crater's rocky zone (Fig. 1b) with an along-profile spacing of 10 m (Fig. 3). For each crater, we manually measured the horizontal distance between the crater rim and the downslope extent of the rocky zone (Fig. 1b), herein referred to as the "rocky zone length", by determining which concentric profile corresponded best to the visual end of the exposed bedrock and taking the profile's distance from the rim. We used the concentric profile that corresponded to the rocky zone length to clip the full-crater polygon into a ring-shaped polygon covering only the rocky zone. Below the rocky zone, the crater walls were typically mantled in sediment—including talus, fan deposits, or other mantling material—and this area is referred to generically as the colluvial zone (Fig. 1b). The colluvial zone is easily distinguished from the rocky zone due to its smooth surface texture. We defined the colluvial zone as the area directly downslope of the rocky zone and made measurements over an area with the same horizontal distance as the rocky-zone length for

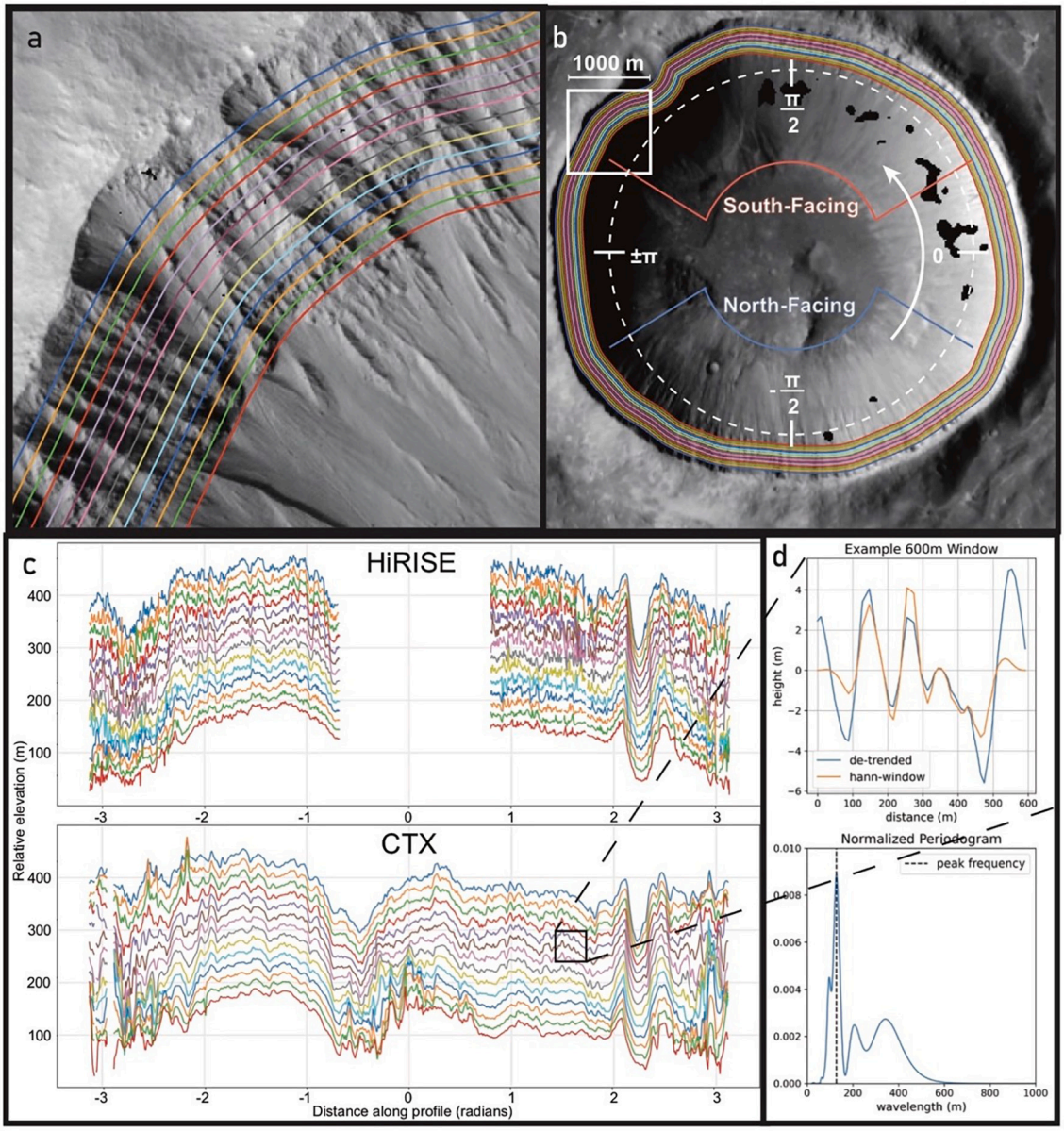

Fig. 3. CTX DEM is used to generate (a) concentric profiles parallel to the rim at a fixed spacing of 25 m down the slope. (HiRISE stereopair ESP_012959_1895_ESP_013104_1895) b) concentric profiles of full crater (CTX Mosaic (Dickson et al., 2018)(c) Topography is extracted along the contours from HiRISE and CTX. (d) Periodograms are extracted from windows in (b) north-facing and south-facing slopes, and peak wavelength and chute relief is measured from the periodogram. (Crater ID - 15-000516).

statistical comparison. We again used the concentric profiles bounding the colluvial zone to generate a ring-shaped polygon covering the colluvial zone.

For each crater, we took measurements of the north and south-facing walls of the crater. Due to the sun-synchronous afternoon orbit of MRO, CTX images outside of polar regions typically have a shadowed east-facing slope and an illuminated west-facing slope. To minimize artifacts from lighting conditions, we defined the northern (south-facing) third as $\pi/6$ to $5\pi/6$ rad from North along the concentric crater profile, and the southern (north-facing) third as $-\pi/6$ to $-5\pi/6$ rad (Fig. 3b). In certain craters, only the north or south facing wall passed filtering due to illumination effects, so there are craters where only one slope is reported. In total, we made measurements of 426 total crater walls in 243 craters (Fig. 2b).

To filter for noise and artifacts in the data, we compared reliability of measurements between consecutive profiles (Fig. 3c). Using the initial profile from the automated rim mapping, we divided each profile into 360 equal length sections in radial coordinates θ. We calculated the average elevation difference between profiles for each section. Our profiles were spaced 25 m horizontally (Fig. 3), and since our measurements show that the crater slopes did not exceed 45°, we expected the average elevation difference D at constant θ to be equal to or less than 25 m, and for profiles further downslope to have lower values of D than those upslope. Values of θ where $D > 25\ m$ or $D < 0\ m$, as well as values of θ with missing data were considered artifacts in DEM generation and excluded from further analysis. We implicitly assumed that the inner crater profiles were downslope of the rim, so in locations where small topographic spurs on the inner profiles are upslope of the outer profiles, the slope is underreported. However, due to the requirements of our rim-finding algorithm, as provided in the supplementary materials, we do not expect local topographic spurs to have had a significant impact on the data.

After filtering out artifacts, we took measurements of chute relief, wavelength and slope from the topography using a method that was

informed by Perron et al. (2008) using Fourier power spectra. Measurements were taken using a sliding window along each concentric profile within the rocky zone. Within the window, the elevation data were detrended by subtracting a linear trend from the values. We applied a Hann windowing function (Press et al., 1992) to the data to smooth edge effects (Fig. 3d), and padded both ends with zeros. By eye, most bedrock chutes had wavelengths <400 m, and so to filter out windowing effects, we ran a Butterworth high-pass filter on the data with a cutoff wavelengths of 400 m. We took the periodogram (P_{DFT}) of the result, applying a correction for the windowing Hann function $W(n)$, $P_{DFT}(k_x) = \frac{|Z(k_x)|^2}{N\sum_{n=0}^{N-1} W(n)}$ (Press et al., 1992), in which $Z(k_x)$ is the Fourier transform of the windowed data of length N. The peak of the periodogram was taken as the peak wavenumber and inverted to find peak wavelength. Chute relief of each window was calculated as twice the amplitude $A = 2\sqrt{\sum P_{DFT}}$ (Perron et al., 2008) (Fig. 3e). A range of window sizes between 100 and 1200 m were tested, and window sizes ranging between 500 and 700 m were found to have consistent, comparable peak wavelength measurements that were on the approximate scale of bedrock features measured manually (Supplementary Section 5.3). We ultimately used the 600 m window for our global analysis.

To further filter out sparse outliers due to errors in estimating the crater rim, chute relief values $> 2\sigma$ away from the mean were excluded from the dataset for each profile, in which σ is the standard deviation of chute relief for each orientation profile. To characterize the slope of the rocky zone, we calculated the median slope from the CTX DEM raster in the area between the rim and the rocky zone boundary using the ArcMap Slope tool (Fig. 4a). We did the same for the colluvial zone (Fig. 1b).

2.4. Bedrock chute measurements using HiRISE

To complement the CTX measurements, we used HiRISE, which has a native resolution of 0.25 m/px (McEwen et al., 2007), to generate high resolution DEMs. Because HiRISE footprints are small relative to CTX, HiRISE DEM coverage of Mars is targeted towards locations of particular geomorphic interest and is thus not ideal for a global survey of entire crater rims. But, where available, HiRISE DEMs provide an alternative metric by which we can assess the reliability of CTX DEMs.

To test the reliability of CTX DEMs in measuring bedrock gully morphology, we performed chute relief, wavelength, and slope measurements at north and south-facing slopes of nine craters using 3 m/px HiRISE DEMs, also generated with ASP. Each HiRISE DEM was aligned with the overlapping CTX DEM using manually determined ground control points (GCP) and a linear shift from the Georeferencing tool in ArcMap that distributes residuals evenly across the GCPs. The same rim-parallel concentric profiles generated from the CTX DEM were used to extract data from the HiRISE DEM at 10-m point spacing (Fig. 3c).

Due to the relatively small footprint of LROC NAC stereo products compared to the size of craters that host bedrock chutes, we were unable to use the automatic tool to make measurements of bedrock chutes on the Moon. Instead, we took measurements of lunar chutes manually. To adequately compare these measurements to the martian chutes and evaluate how manual measurements compared to those generated from spectral analysis, we also manually measured the chute relief, wavelength, and slope of characteristic bedrock chutes of six craters with HiRISE DEM coverage (Fig. 2b). We used 3 m/px HiRISE DEMs to generate equipotential contours spaced at 15 m of elevation. This resolution was chosen for processing efficiency given the scale of our study and that it satisfied our specific measurement needs. We drew piecewise linear profiles in planview across a series of 4–5 chutes with the points located on the same topographic contour line and at the ridges in between the chutes (Fig. 5). We extracted the topography along the profiles and manually measured the wavelength as the average horizontal distance between ridges, and the chute relief as the average peak-to-valley elevation difference. We also used the same spectral technique from Section 2.3 to extract chute relief and wavelength for the same profiles.

To compare to the measured slopes of the rocky zone, we took manual measurements of the slope of the longitudinal profile from all nine craters with HiRISE DEMs. We drew linear profiles by eye down the middle of the bedrock chutes perpendicular to the topographic contours (Fig. 4b). We extracted topography along these profiles and found a best-fit topographic slope by fitting a line (by least squares) using a sliding window of 100 m along the profile. We reported the slope of the profile as the median of the windowed values.

2.5. Lunar survey and measurements

We conducted a semi-automated survey for lunar bedrock chutes by using data from the Kaguya Terrain Camera (Kato et al., 2010) to generate a global 10 m/px slope map. We isolated locations where pixels with slopes between 30°-40° were clustered in polygons of area greater than 60,000 m^2. This effectively mapped the rim crests of fresh lunar craters. We cross-compared these regions with all locations that have LROC NAC (Robinson et al., 2010) stereo coverage, resulting in 403 locations (Fig. 2a).

Each of the 403 locations were visually inspected for the presence of chutes and exposed bedrock. Nineteen craters had bedrock chutes observable in LROC NAC imagery. We used ASP (Beyer et al., 2018) on LROC NAC pairs with adequate lighting and coverage for stereo photogrammetry to generate 1.5 m/px DEMs (Supplementary Materials Section 4) of craters with exposed bedrock. We made measurements at six locations that had adequate DEM coverage of portions of crater walls with three or more bedrock chutes. We measured chute morphology

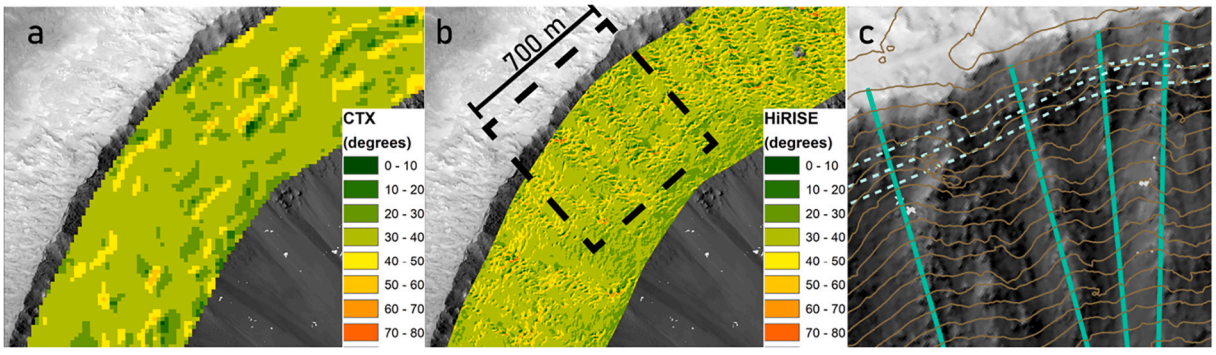

Fig. 4. Slope calculated from a) CTX DEM (G19_025514_2048_XN_24N252W and G20_025870_2048_XN_24N252W) and b) HiRISE DEM (ESP_026292_2045 and ESP_026015_2045) using the *arcpy* Slope tool. Black dashed box is enlarged in c) to show profiles drawn manually to measure chute depth (dashed) and slope (solid cyan) over topographic contours (brown lines) extracted from HiRISE DEM. (Crater ID: 14–000645). (For interpretation of the references to colour in this figure legend, the reader is referred to the web version of this article.)

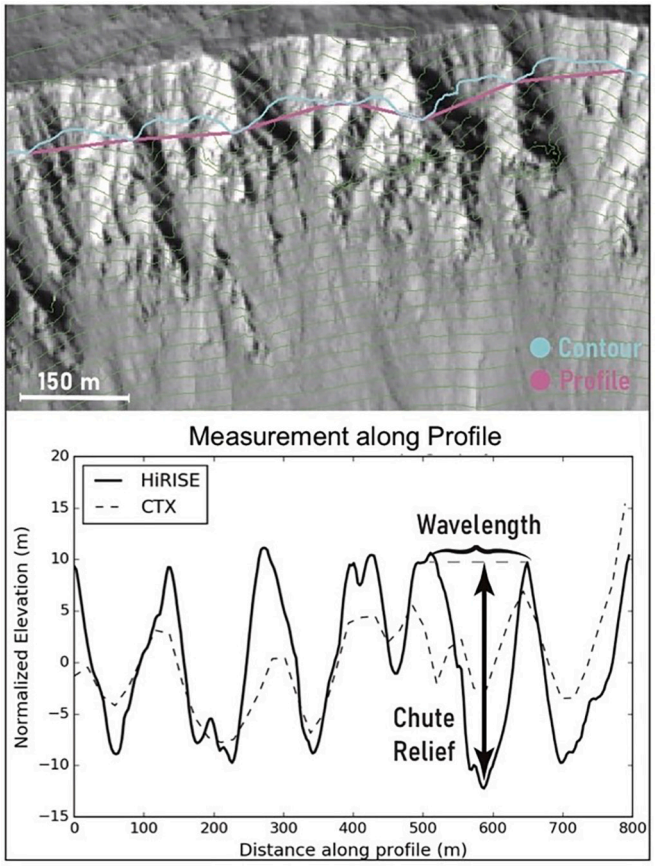

Fig. 5. Topographic contours (solid green lines) were generated from HiRISE DEM (ESP_020667_2190 and ESP_020245_2190). An example profile (magenta) is drawn to connect ridges along an example topographic contour (cyan), and topography is extracted along this profile using HiRISE and CTX DEMs. (Crater ID: 04–001128). (For interpretation of the references to colour in this figure legend, the reader is referred to the web version of this article.)

(wavelength, chute relief, and slope) by extracting profiles manually using the topographic contour method (Fig. 5), as described for the HiRISE DEM measurements (Section 2.4). Manual measurements were necessary for the LROC NAC DEMs; due to the unavoidable illumination variability between potential NAC stereo pairs, any DEM is susceptible to missing data, especially due to shadow-related artifacts in areas of sharper topography.

3. Results

3.1. Lunar survey and measurements

Out of the 403 craters we surveyed on the Moon, only nineteen craters (2%) had bedrock chutes observable in LROC NAC imagery. For these nineteen craters, we observed exposed bedrock in two broad morphologic categories: small, individual exposed bedrock scarps on mostly regolith-covered slopes (Fig. 6c), and larger exposed bedrock escarpments along crater rims (Fig. 6a). Both types of exposures tended to be located near the crater rim, where slopes are high (~40°). The exposed edges of rocky layers midway down the slope appeared rough and weathered, possibly serving as a source of debris (Fig. 6c). In some cases, evidence of downslope movement was observed in the form of debris avalanches directly below the scarp, boulder deposits at the bottom of the crater wall, and boulder tracks. A particularly striking example of a debris channel is shown in Fig. 6d; it has well-defined levees and is downslope of rough, exposed bedrock on a steep slope (Supplementary Section 2).

In some locations, many small bedrock chutes were observed on the same crater wall (Fig. 6a). These chutes are fairly short, narrow and parallel to one another, and are just barely resolved in LROC NAC stereo topography. A single crater can have many instances of small bedrock chutes (Fig. 6a), or just one or two groups of chutes in isolated exposures of bedrock on an otherwise smooth slope (Fig. 6b).

In one crater out of the 403 surveyed, we observed multiple bedrock chutes coalescing into a feature reminiscent of a martian gully alcove, with a roughly amphitheater shape (Fig. 6b). This “alcove” had a maximum relief of 25 m, much larger than the average lunar chute, and closer in scale to gully alcoves on Mars. However, deeply incised and sinuous gully channels, like those observed on Mars (Malin and Edgett, 2000; Harrison et al., 2015), were not observed in any of the craters we surveyed on the Moon.

Due to the small size of the lunar chutes, and the difficulty of producing stereo products with LROC NAC due to irregular lighting, we measured four chutes in each of six craters (Fig. 2a). The median depth of these resolvable chutes on the Moon was 5.0 m (IQR = 4.25–6.25), and the median wavelength was 70 m (IQR = 40–100). Lunar chutes had slopes ranging from 38.5° to 43.4°.

3.2. Mars survey

Compared to the Moon, Mars has many more occurrences of bedrock chutes with a wider range of chute morphologies. There are well-incised chutes—bedrock chutes with margins clearly defined by linear topographic highs—some of which contain within them networks of nested smaller chutes (Fig. 7a, c). Large bedrock chutes that do not host nested chutes exhibit smooth floors without exposed bedrock (Fig. 7b). Other landforms resemble chutes but have a more muted or diffuse topographic expression (Fig. 7d).

Well-incised bedrock chutes were observed at all latitudes. Well-incised bedrock chutes that merge with well-incised gully channels (Fig. 7a, b) are observed only in the mid-latitudes (30° - 60°). These gully channels are sinuous with sharply defined edges that incise the coherent ice-cemented material draped on the crater wall, as well as pre-existing debris fans (Christensen, 2003). In contrast, bedrock chutes in the equatorial region have softer edges, are not sinuous, and do not terminate with large debris fans (Fig. 7c).

3.3. Mars global measurements

Based on our observations, we categorized each crater-wall by orientation and the presence (Fig. 7a, b) or absence (Fig. 7c, d) of incised gully channels in the colluvial zone resulting in four categories: (1) North-facing crater walls with gully channels, (2) north-facing walls without gully channels, (3) south-facing walls with gully channels, and (4) south-facing walls without gully channels. Data (chute relief, wavelength, slope, and rocky zone length) from each category was separated into 10-degree bins and plotted against latitude and orientation (Fig. 8).

From our global CTX survey, chute-relief values (Fig. 8a) range from 5.5 m to 64.2 m with a global median value of 12.5 m (IQR 10.1–16.2 m). Median chute-relief values per latitude bin for both south-facing and north-facing walls steadily increase between 5°S and 30°S. Orientation disparities within craters were observed in chute relief measurements in bins extending from latitudes as high as 50°S and as low as 10°S, where south-facing (pole-facing) walls had consistently larger chute relief values than north-facing (equator-facing) walls. The orientation disparity between chute relief on north and south-facing slopes is statistically significant ($p < 0.05$) in the 20°S-10°S bin without gully channels, and in the 30°N-40°N bin with gully channels (see Supplementary Materials). The 30°S-20°S bin likely has too few data points for statistical significance. The highest chute-relief values were measured on south-facing walls with gully channels in the southern hemisphere. In the northern hemisphere, chute relief values are clustered around the

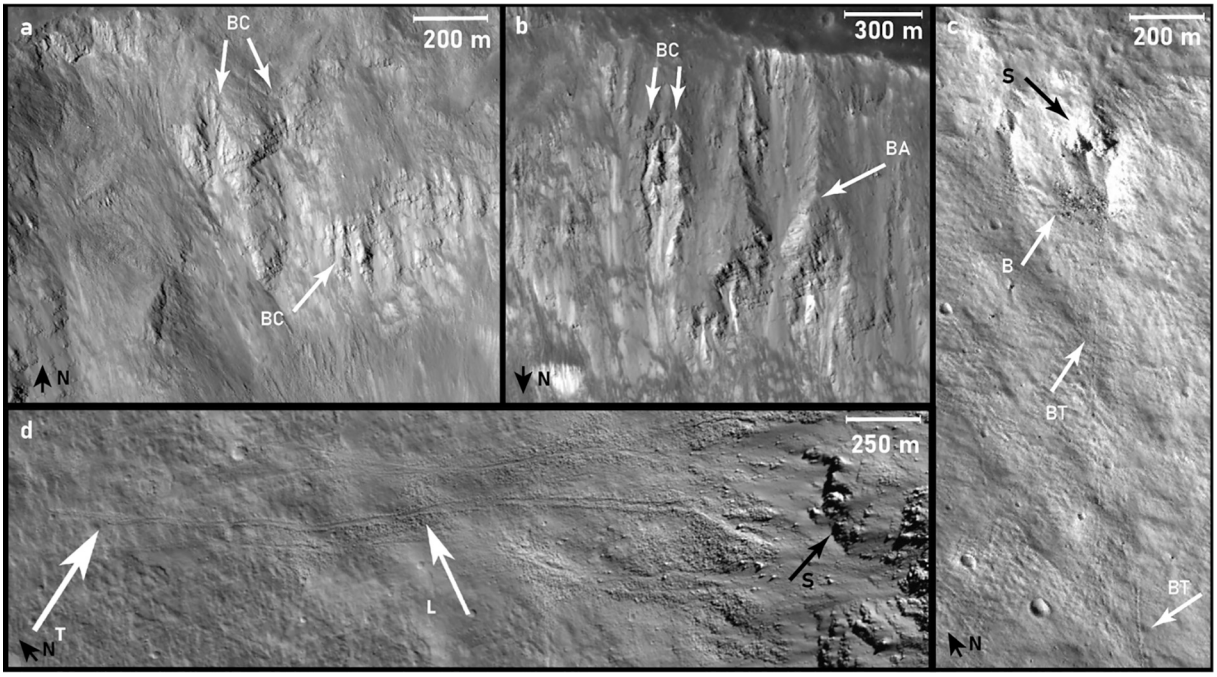

Fig. 6. Bedrock erosion observed on steep lunar slopes. (a) Narrow, shallow bedrock chutes (BC) are found on exposed rocky midslope scarp –(LROC NAC M104819973R GSFC/ASU/MSSS). (b) The largest chute we observed in our survey was found on (LROC NAC M190294287L GSFC/ASU/MSSS), and was the only location in our lunar survey where we observed a feature (BA) similar to martian alcoves (roughly 25 m deep). (c) Observed evidence of downslope erosion are boulder deposits (B) below exposed scarps (S), as well as boulder tracks (BT) (LROC NAC M1126054875L GSFC/ASU/MSSS). (d) Several instances of leveed debris channels were observed originating at rocky scarps (S), and featuring visible levees (L) and a lobate toe (T) (LROC NAC M1137352726L GSFC/ASU/MSSS).

global median, with no easily discernible trend with orientation.

Chute wavelength values (Fig. 8b) range between 209 m and 334 m, with a global median value of 297 m (IQR = 287–307 m). Note that these measurements were made after applying a high pass filter, reducing the influence of wavelengths >400 m. Median values for each latitude bin are clustered around the global median. There is a weak orientation dependence observed in wavelength in bins between 10°S - 30°S, with north-facing (equator) walls measuring larger median wavelengths than the south (pole) facing walls by ~10 m (Fig. 8b). South-facing walls with gully channels in the southern hemisphere host bedrock chutes with the smallest wavelengths. Chute relief and wavelength are correlated ($R = -0.4$, $p = 2 \times 10^{-26}$), with larger chute relief values corresponding with smaller wavelength values.

Slope values for the rocky zone (Fig. 8c) range between 25° and 45° with a global median value of 33°. Rocky zone length (Fig. 8d) ranges between 125 m and 800 m with a global median value of 300 m. This lengthscale is constrained by the crater sizes we analyzed. Rocky zone slope is not correlated with rocky zone length ($R = -0.18$, $p = 1 \times 10^{-4}$), nor is it correlated with orientation or presence of gully channels (Fig. 8). Median rocky zone length for crater walls with gully channels is greater than for cases without gully channels, but does not have an orientation preference.

Colluvial zone slopes range between 22° and 41° with a global median value of 31°, and are strongly positively correlated ($R = 0.76$, $p = 2 \times 10^{-83}$) with the corresponding rocky zone slopes (Fig. 9). Rocky zones are consistently steeper than colluvial zones by a few degrees. For a given rocky slope, corresponding colluvial slopes without gully channels tend to be steeper than those with gully channels (Fig. 9).

3.3.1. Comparison to HiRISE

Chute relief, wavelength, and topographic slope measurements made using CTX data are positively correlated with those made with HiRISE data (Fig. 10). Due to the higher spatial resolution of HiRISE, HiRISE DEMs more accurately represent morphologies of smaller chutes than CTX (Fig. 5). However, HiRISE data is more affected by artifacts caused by strong shadows in rough topography within bedrock chutes. Broadly, CTX data shows the same trends in chute relief, wavelength, and slope as observed in HiRISE data, raising confidence in the global trends in these features measured using CTX.

HiRISE manual and automated chute-relief measurements also are well correlated ($R = 0.92$, $p = 0.0098$). Manual chute-relief measurements are slightly larger than the corresponding automated measurement (Fig. 10a). Manual and automated wavelength measurements are uncorrelated (R = -0.13, $p = 0.80$), and manual wavelength measurements tended to be smaller than corresponding automated wavelength measurements (Fig. 10b). These findings are consistent with expectations; manual measurements specifically targeted visible bedrock chutes, while automated measurements fold in non-chute topography (e.g., the background crater topography), which skews the wavelength measurements large, and smooth terrain, which lowers the average of chute relief. The chute slope measurements made using HiRISE by manually delineating the chute centerline versus those made using the arcpy slope tool in the rocky zone were positively correlated ($R = 0.69$, $p = 0.04$) and comparable, although the manual measurements show less variability (Fig. 10c).

3.4. Comparing Martian and lunar chutes

In order to quantitatively test for a morphological trend depending on likelihood of volatile activity, we chose three categories of martian observations to compare to the lunar chutes. Sinuous gully channels in the martian mid-latitudes are inferred to form through volatile processes (Malin and Edgett, 2000; Dundas et al., 2010), so we treated both north and south-facing locations with incised gully channels emanating from bedrock chutes as a potential "wet" endmember, where volatile activity is likely to have been involved. Mid-latitude pole-facing slopes without gully channels are locations where gully channels could be expected (Harrison et al., 2015), so they were chosen as the next "drier" category. We chose equatorial slopes between 5°S and 5°N as locations that do not host features known to be associated with Amazonian volatile activity

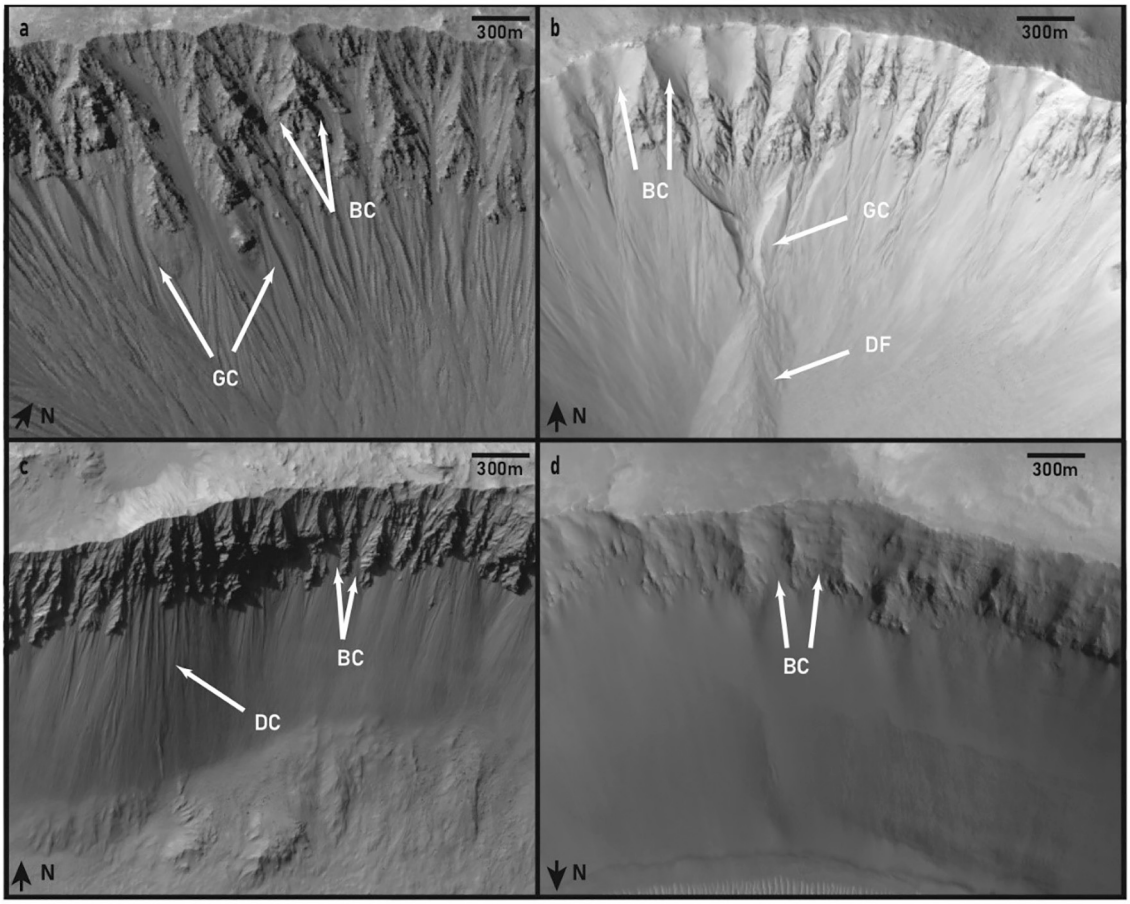

Fig. 7. We classified martian slopes with bedrock chutes (BC) based on orientation, latitude, and sedimentary zone incision. (a) Locations with sinuous gully channels (GC) incised deeply into the sediment (HiRISE Image: ESP_025716_2200 NASA/JPL-Caltech/UoA) or (b) large, incised gully channels with large depositional fans (DF) (HiRISE Image: ESP_019438_2340 NASA/JPL-Caltech/UoA) are assumed to be locations where recent volatile activity is more likely. Locations without incised channels can have (c) well incised bedrock chutes and debris chutes (DC) (HiRISE Image: ESP_016196_1605 NASA/JPL-Caltech/UoA) or (d) very poorly defined or potentially filled in chutes (HiRISE Image: ESP_019307_1715 NASA/JPL-Caltech/UoA).

on steep slopes. We compared the chute relief across these categories (Fig. 11a) and found that the deepest bedrock chutes were found in the category with incised gully channels, corresponding with the highest likelihood of volatile activity. In terms of chute relief, midlatitude chutes (with and without gully channels) are statistically distinct from equatorial chutes (Mann-Whitney $U = 2006.0$, $p < 0.05$, $n_{midlat} = 99$, $n_{equator} = 66$).

The mean chute relief of lunar chutes is 5 m, shallower than all three categories of martian chutes. However, lunar chutes are considerably steeper than their martian counterparts, with median slopes ranging from 38.5° to 43.4°. The bedrock chute slopes for the three martian categories, in contrast, average only 33° and show no strong trend with location category.

4. Discussion

4.1. Bedrock chute formation by dry processes

Bedrock chutes on the Moon (Figs. 1a, 6) presumably formed through dry processes such as rockfall and dry debris avalanches (Bart, 2007; Beer et al., 2020; Kokelaar et al., 2017; Kumar et al., 2013; Sun et al., 2021). We observed nineteen locations on the Moon where midslope bedrock outcrops were incised by a series of chutes (Fig. 2a). Most of the chutes we observed were shallow—no more than 10 m in depth – and we measured the most prominent chutes available. A possible explanation for the scarcity of lunar chutes, especially when compared to their martian counterparts, is that chute formation is infrequent in the absence of volatile activity. Another possibility is that more lunar chutes exist, but they are concealed under a layer of regolith that rarely exposes the upper walls of impact craters (e.g., Stopar et al., 2017). We also found that lunar bedrock chutes preferentially (though not exclusively) form in mare units (Fig. 2), which suggests a possible lithologic control in either chute formation or in regolith cover.

Some rocky outcrops on the Moon co-occur with evidence for downslope debris movement such as leveed channels and debris fans (Kokelaar et al., 2017) (Fig. 6c, d). Some of these landforms have alcove-channel-fan organization similar to that of martian gullies (Bart, 2007). These landforms—including even the most prominent leveed debris chute (Fig. 6d)—did not have topography observable in the 1.5 m/px DEMs, leading us to conclude that these are shallow channels. Unlike martian midlatitude gully channels which typically incise into ice-cemented regolith (Christensen, 2003), the lunar landforms likely form within loose regolith, which would lack the strength to support well incised channels. Similar features are observed on Mars in areas such as Nirgal Vallis, for example, where channels form in loose regolith (e.g., Malin and Edgett, 2000; Reiss et al., 2004).

The single alcove-like landform we observed among our target craters on the Moon is 25 m deep (Fig. 6b), though other lunar alcoves have been observed in previous studies (See Fig. 3, Fig. 14 in Kumar et al., 2013). Considering that only one out of the 403 craters we surveyed contained such an alcove, we inferred that exposed bedrock chutes with relief of 20 m or more are rare on the Moon. There may be other factors

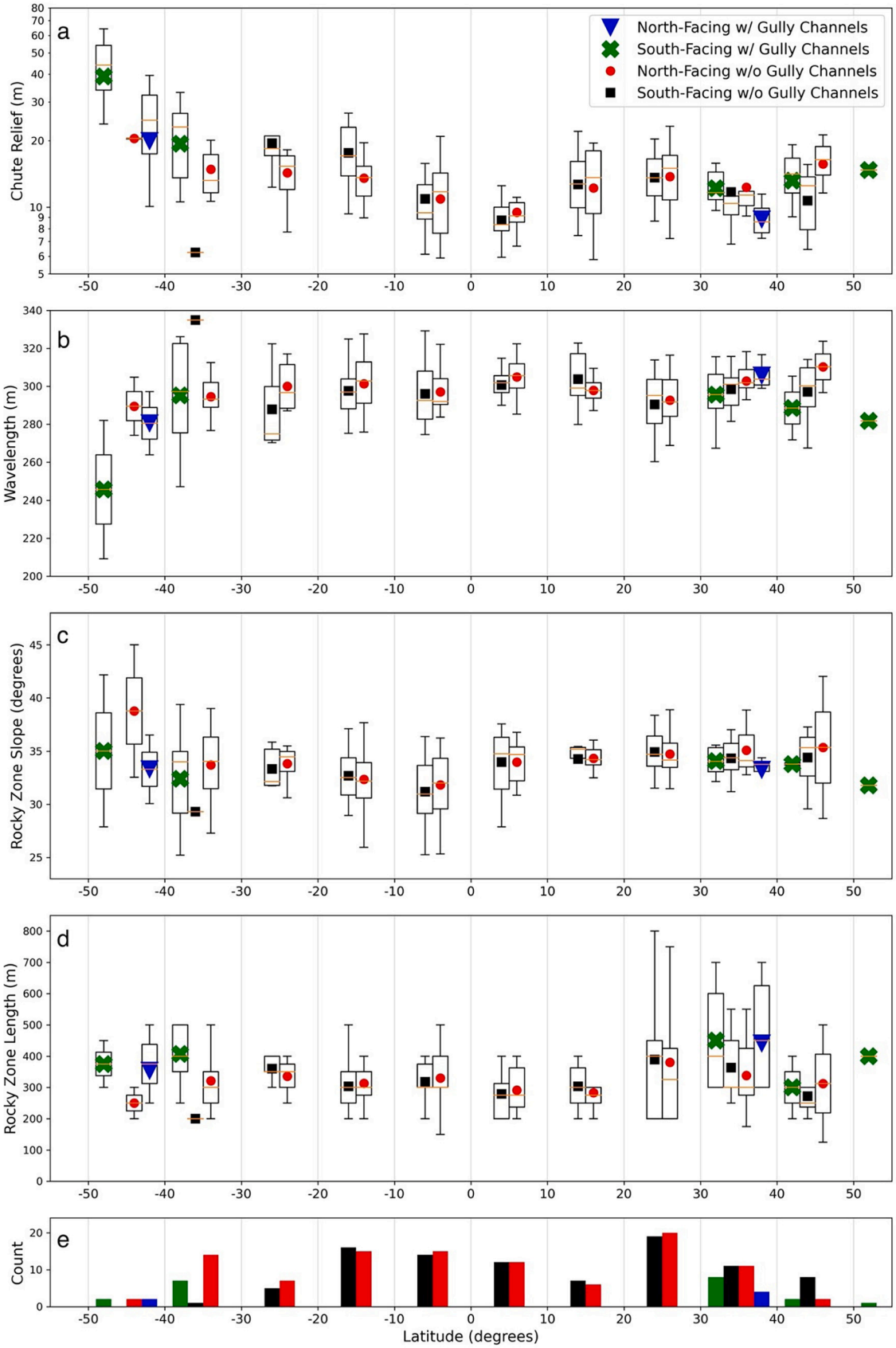

Fig. 8. Data from global CTX measurements was split into four categories (north and south facing with or without the presence of gully channels. Data from each category was binned by 10° latitude bins and the median, IQR, and range of measurements for each bin was plotted as a box plot for a) chute relief, b) chute spacing (or wavelength), c) slope of the rocky zone, and d) length of the rocky zone. The mean value per category per bin was plotted as a symbol. Panel (e) shows the number of observations per category.

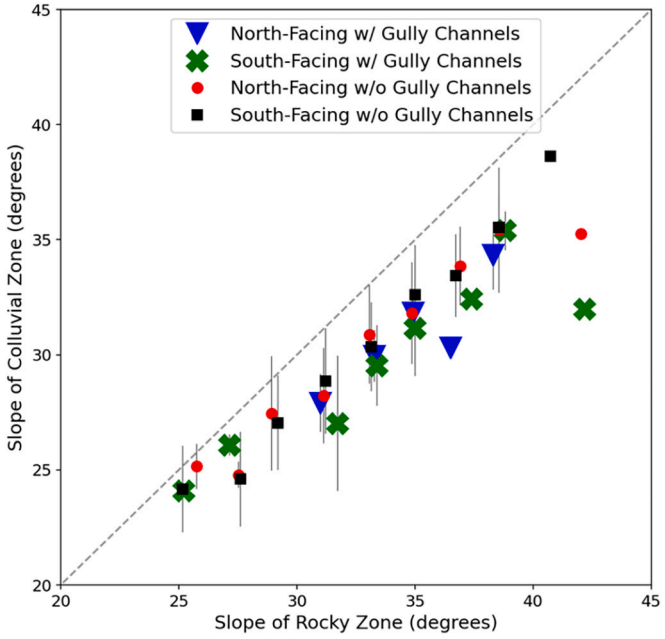

Fig. 9. Slopes of rocky zones were binned by 2° latitude per category and plotted against corresponding colluvial zone slopes. Steeper rocky zones correlate strongly with steeper colluvial zones.

that hinder the formation of bedrock chutes on the Moon, such as the comparatively high rate of degradation of crater rims on the Moon through non-local processes such as small impacts and regolith filling processes (Fassett and Thomson, 2014) and the high production rate of lunar regolith (Watkins et al., 2019). Nevertheless, our observations provide constraints on the degree of channelization that can be expected by dry processes on an airless body with steep slopes and significant gravity, such as the Moon. Importantly, bedrock channelization, although rare on the Moon, need not be associated with volatile activity.

Our survey of bedrock chutes on Mars showed a large spectrum of morphologies, ranging from shallow (Fig. 7d) to deeply incised chutes (Fig. 7a,b,c). Morphologically, the shallow bedrock chutes observed in some equatorial craters (Figs. 1b, 7d) are the most like those observed on the Moon. This comparison suggests that bedrock chutes formed by dry processes might also occur on Mars in certain environments. However, our results suggest that there might be a limit to how deeply chutes can be carved by dry processes alone.

Our analysis from the Moon is consistent with previous work (Bart, 2007; Kokelaar et al., 2017; Kumar et al., 2013) that shows that completely dry processes can erode bedrock on steep slopes. On Mars, erosion by volatile-related processes and by completely dry processes are not mutually exclusive, and it is possible that dry processes have contributed to bedrock erosion at all of our study sites across the planet. Our results show that volatile-related processes are likely more significant, but a more precise comparison between wet and dry proceses is not attainable with current data.

4.2. *Bedrock chute formation with volatiles*

Well incised, deep bedrock chutes on Mars appear to be tied to the presence of volatile activity, based upon their distribution and orientation preference for cold slopes. On Mars, chute relief shows an orientation dependence in the southern hemisphere (Fig. 8a), with deeper chute relief measurements on pole-facing (south-facing) slopes than on their equator-facing counterparts. This observation is congruent with the fact that martian gullies form preferentially on midlatitude pole-facing slopes (Dickson et al., 2007; Heldmann and Mellon, 2004). Furthermore, chutes on midlatitude pole-facing slopes with gully channels (Fig. 7a) tend to be deeper than chutes on midlatitude pole-facing slopes without gully channels (Fig. 11a). These observations implicate volatile processes in the formation or evolution of deep bedrock chutes. Because our measurements were targeted towards young, fresh craters, the chutes in our study most likely indicate volatile activity that occurred in the Late Amazonian period.

Gully channels in the southern hemisphere are primarily observed between 30°S and 60°S (Harrison et al., 2015). However, the orientation disparity we measured in bedrock chute relief continues consistently to latitudes as low as 10°S (Fig. 8), within the contemporary tropics, where well-incised gully channels and aprons are not observed (Balme et al., 2006; Dickson et al., 2007; Harrison et al., 2015; Heldmann and Mellon, 2004; Kneissl et al., 2010; Malin and Edgett, 2000; Milliken et al., 2003). This observation is evidence that volatiles in some capacity might have been active at lower latitudes on Mars than is apparent from the record of martian gully occurrence. Bedrock chutes are carved into rock, and it presumably takes more time to form chutes in rock than to form gullies in sediment. Some equatorial craters with intact rims have well incised bedrock chutes with orientation disparities (i.e. Fig. 12.); thus, volatile activity must have persisted for long enough to carve chutes into rock at locations where even seasonal H_2O and CO_2 frost is not observed today (Schorghofer and Edgett, 2006).

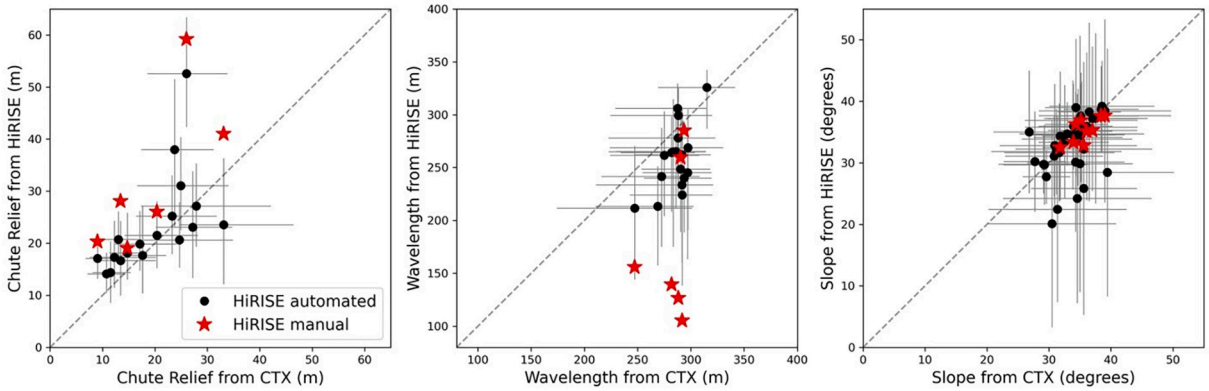

Fig. 10. Automated HiRISE and CTX measurements were taken on north and south-facing slopes of 9 craters. There are a) two automated chute relief measurements, b) two automated chute wavelength measurements, and c) four automated chute slope measurements per crater (black circles). For each automated location, values are represented as a median with the interquartile range as the error bar. Manual measurements (red stars) of chute relief and wavelength were made on six of the same craters and manual measurements of slope were made on all nine craters using HiRISE to verify the automated method. Manual values are presented here as the mean of measurements made on each slope. (For interpretation of the references to colour in this figure legend, the reader is referred to the web version of this article.)

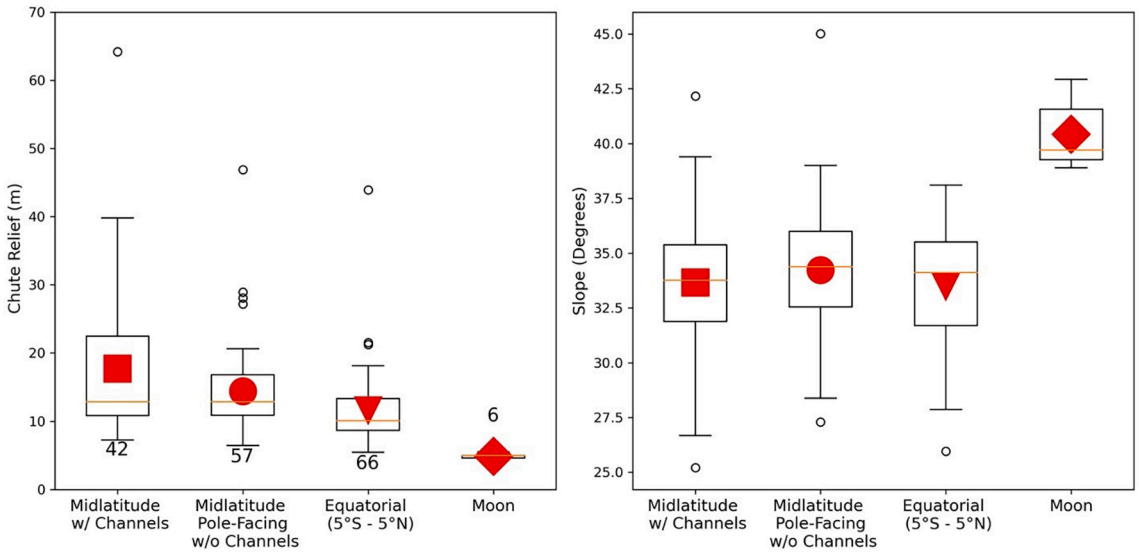

Fig. 11. Distributions of mean chute relief and chute slope values for four categories of crater with different inferred volatile presence (Mars Mid- latitude with incised gully channels, midlatitude pole-facing without gully channels, tropical, and Moon), are plotted as box plots (median, IQR, range, and outliers) with symbols representing the mean values. Populations of each category are indicated numerically next to the chute relief box plots.

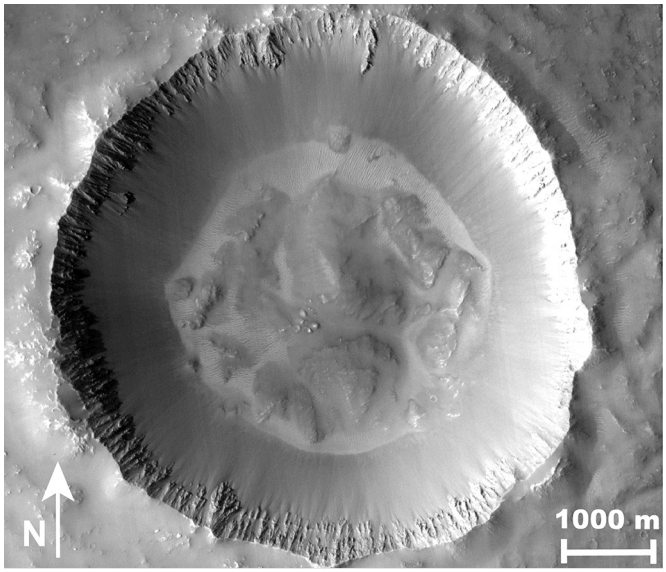

Fig. 12. Crater 20-001961. Equatorial crater (1°S) with distinct, regular bedrock chutes.
Image: CTX Mosaic (Dickson et al., 2018).

The northern hemisphere does not exhibit as clear a trend in chute relief versus latitude and orientation as in the southern hemisphere. A similar hemispheric bias has been observed for martian gullies, which is partly due to a paucity of steep slopes (Conway et al., 2019b; Heldmann and Mellon, 2004; Malin and Edgett, 2000). Northern gullies also appear more degraded (Heldmann et al., 2007) and are generally less active (Dundas et al., 2010) than their southern counterparts. The present-day larger seasonal extremes in the southern hemisphere due to Mars' current orbital eccentricity allow for more dynamic CO_2 activity at lower latitudes in the southern hemisphere (Toon et al., 1980). However, at different orbital configurations achieved within the last million years (Laskar et al., 2002), CO_2 is expected to have been similarly active in the northern hemisphere (Mischna et al., 2003; Schorghofer and Edgett, 2006). In part, the shallower depth of bedrock chutes in the northern hemisphere could be attributed to regional differences in the "strength" of the underlying terrain, which has been shown to have an effect on the overall crater shape (Herrick and Hynek, 2017). Based upon our observations of abundant smooth floors within chutes in the northern hemisphere, another possible explanation is that those chutes are partially filled by mantling material (Fig. 7b) (Kreslavsky and Head, 2000). There is evidence of more recent ice-mantling deposits in the northern hemisphere, where the material is particularly homogeneous (Kostama et al., 2006).

Unlike well-incised gully channels, bedrock chutes are found at all latitudes on Mars making them a potentially useful landform for inferring relative volatile activity (Fig. 2b). Two factors implicate a role of volatiles in their formation: (1) chute relief on Mars is a function of latitude (Fig. 8a), a pattern we did not observe for chutes on the Moon, which were also shallower than their martian counterparts, and (2) chutes exhibit orientation preferences for cold, pole-facing slopes extending to the contemporary tropics, which is challenging to explain through processes that do not include volatiles as, at minimum, a triggering event for rockfall. Rockfall on crater slopes triggered by processes that do not involve the phase transitions of volatiles, such as solar-induced thermal stresses, have been shown to be biased towards warmer, sunlit slopes in the tropics (Tesson et al., 2020), which is the opposite of the pattern we observe.

Though it is not observed at low latitudes in present day conditions, during periods of increased obliquity, H_2O ice at the surface becomes unstable at the poles and is redeposited at lower latitudes (Head et al., 2003). Our results suggest that tropical pole-facing slopes in the southern hemisphere at high-obliquity may have behaved similarly to mid-latitude pole-facing slopes at lower obliquity, like today, where CO_2 and H_2O ice are more capable of accumulating. This behavior could be recorded in the patterns in the level of incision of bedrock.

5. Conclusions

Bedrock chutes and alcoves are found on exposed crater rims of fresh impact craters at all latitudes on Mars. Observations of presumably volatile-free bedrock chutes on the Moon show that bedrock chutes and at least one alcove can form through dry processes. Thus, dry rockfall might be responsible for some of the bedrock chutes on Mars. On Mars, however, chutes are far more abundant, and many are more incised than those on the Moon, especially outside of the tropics, with orientation-dependent trends that suggest volatile influence in their development.

Chutes on Mars also tend to have lower gradients than on the Moon but are still steep enough (~33°) such that dry rockfall could play a role in chute formation. Further work can be done to explain the distribution and morphologies of lunar chutes by testing factors such as underlying lithology and local regolith thickness.

We observed that pole-facing slopes on Mars have deeper bedrock chutes than equator-facing slopes between 30°S-10°S, which is an equatorward extension of the trend of gullies almost exclusively forming on pole-facing slopes from 30°S-40°S. These observations tie the incision of some bedrock chutes and alcoves to volatile processes that might be similar to the processes involved in the formation of gully channels. Trends in bedrock chute relief might be a useful metric for studying climatic conditions in Late Amazonian Mars, when deposition, accumulation, flow and potentially melting of H_2O-ice was likely achievable at considerably lower latitudes than it is today, in addition to CO_2 frost/defrosting processes.

Our results suggest climatic processes influenced the erosion of some bedrock chutes on Mars but we cannot differentiate among different ice-related mechanisms/flows for triggering mobilization or transporting sediment. Further testing can be done to investigate bedrock chute depth in locations with known recent crater rim glaciation, as demonstrated by Conway et al., 2018. Climate models could also be used to inform the likelihood of explosive CO_2 jetting or destabilization of dry material due to defrosting (Pilorget and Forget, 2016; Sylvest et al., 2016; Kieffer et al., 2006). Compared to transient gully channels, bedrock chutes might be longer lived and thus contain climate information dating back to the formation of the host impact crater itself.

Declaration of Competing Interest

None.

Acknowledgments

We thank Susan Conway and Senthil Kumar for thoughtful and detailed reviews that improved the quality of this paper. This work was supported by NASA Grant 80NSSC19K1269 to MPL. We thank the Student Undergraduate Research Fellowship (SURF) at Caltech for their support with this project, and the Columbia University Work Exemption Program for additional funding. We appreciate Caleb Fassett for providing the majority of Mars DEMs used in this study.

Appendix A. Supplementary data

Supplementary data to this article can be found online at https://doi.org/10.1016/j.icarus.2021.114774.

References

Armitage, J.J., Warner, N.H., Goddard, K., Gupta, S., 2011. Timescales of alluvial fan development by precipitation on Mars. Geophys. Res. Lett. 38 https://doi.org/10.1029/2011GL048907.

Auld, K.S., Dixon, J.C., 2016. A classification of martian gullies from HiRISE imagery. Planet. Space Sci. 131, 88–101. https://doi.org/10.1016/j.pss.2016.08.002.

Balme, M., Mangold, N., Baratoux, D., Costard, F., Gosselin, M., Masson, P., Pinet, P., Neukum, G., 2006. Orientation and distribution of recent gullies in the southern hemisphere of Mars: observations from high resolution stereo camera/Mars express (HRSC/MEX) and Mars orbiter camera/Mars global surveyor (MOC/MGS) data. J. Geophys. Res. Plan. 111 https://doi.org/10.1029/2005JE002607.

Bart, G.D., 2007. Comparison of small lunar landslides and martian gullies. Icarus 187, 417–421. https://doi.org/10.1016/j.icarus.2006.11.004.

Beer, A.R., Ulizio, T.P., Ma, Z., Fischer, J., Lamb, M.P., 2020. Bedrock Topographic Evolution from Rockfall Erosion, EGU General Assembly 2020, Online, 4–8 May 2020, EGU2020–12980. https://doi.org/10.5194/egusphere-egu2020-12980.

Beyer, R.A., Alexandrov, O., McMichael, S., 2018. The Ames stereo pipeline: NASA's open source software for deriving and processing terrain data. Earth Space Sci. 5, 537–548. https://doi.org/10.1029/2018EA000409.

Christensen, P.R., 2003. Formation of recent martian gullies through melting of extensive water-rich snow deposits. Nature 422, 45–48. https://doi.org/10.1038/nature01436.

Conway, S.J., Butcher, F.E.G., Haas, T., Deijins, A.A.S., Grindrod, P.M., Davis, J.M., 2018. Glacial and gully erosion on Mars: a terrestrial perspective. Geomorphology 318, 26–57. https://doi.org/10.1016/j.geomorph.2018.05.019.

Conway, S.J., de Haas, T., Harrison, T.N., 2019a. Martian gullies: a comprehensive review of observations, mechanisms and insights from earth analogues. Geol. Soc. Lond. Spec. Publ. 467, 7–66. https://doi.org/10.1144/SP467.14.

Conway, S.J., Harrison, T.N., Soare, R.J., Britton, A.W., Steele, L.J., 2019b. New slope-normalized global gully density and orientation maps for Mars. Martian Gullies Earth Analogues. https://doi.org/10.1144/SP467.3.

Costard, F., Forget, F., Mangold, N., Peulvast, J.P., 2002. Formation of recent Martian debris flows by melting of near-surface ground ice at high obliquity. Science 295, 110–113. https://doi.org/10.1126/science.1066698.

Craddock, R.A., Howard, A.D., 2000. Simulated degradation of lunar impact craters and a new method for age dating farside mare deposits. J. Geophys. Res. Plan. 105, 20387–20401. https://doi.org/10.1029/1999JE001099.

Dickson, J.L., Head, J.W., 2009. The formation and evolution of youthful gullies on Mars: gullies as the late-stage phase of Mars' most recent ice age. Icarus 204, 63–86. https://doi.org/10.1016/j.icarus.2009.06.018.

Dickson, J.L., Head, J.W., Kreslavsky, M., 2007. Martian gullies in the southern mid-latitudes of Mars: evidence for climate-controlled formation of young fluvial features based upon local and global topography. Icarus 188, 315–323. https://doi.org/10.1016/j.icarus.2006.11.020.

Dickson, J.L., Head, J.W., Goudge, T.A., Barbieri, L., 2015. Recent climate cycles on Mars: stratigraphic relationships between multiple generations of gullies and the latitude dependent mantle. Icarus 252, 83–94. https://doi.org/10.1016/j.icarus.2014.12.035.

Dickson, J.L., Kerber, L.A., Ehlmann, B.L., 2018. A global, blended CTX mosaic of Mars with vectorized seam mapping: a new mosaicking pipeline using principles of non-destructive image editing. LPSC (2018) 49, 2480.

Diniega, S., Byrne, S., Bridges, N.T., Dundas, C.M., McEwen, A.S., 2010. Seasonality of present-day Martian dune-gully activity. Geology 38, 1047–1050. https://doi.org/10.1130/G31287.1.

Dundas, C.M., McEwen, A.S., Diniega, S., Byrne, S., Martinez-Alonso, S., 2010. New and recent gully activity on Mars as seen by HiRISE. Geophys. Res. Lett. 37 https://doi.org/10.1029/2009GL041351.

Dundas, C.M., Diniega, S., Hansen, C.J., Byrne, S., McEwen, A.S., 2012. Seasonal activity and morphological changes in martian gullies. Icarus 220, 124–143. https://doi.org/10.1016/j.icarus.2012.04.005.

Dundas, C.M., Diniega, S., McEwen, A.S., 2015. Long-term monitoring of martian gully formation and evolution with MRO/HiRISE. Icarus Dynam. Mars 251, 244–263. https://doi.org/10.1016/j.icarus.2014.05.013.

Fassett, C.I., Thomson, B.J., 2014. Crater degradation on the lunar maria: topographic diffusion and the rate of erosion on the moon. J. Geophys. Res. Plan. 119, 2255–2271. https://doi.org/10.1002/2014JE004698.

Golombek, M.P., Warner, N.H., Ganti, V., Lamb, M.P., Parker, T.J., Fergason, R.L., Sullivan, R., 2014. Small crater modification on Meridiani Planum and implications for erosion rates and climate change on Mars. J. Geophys. Res. Plan. 119, 2522–2547. https://doi.org/10.1002/2014JE004658.

Harrison, T.N., Osinski, G.R., Tornabene, L.L., Jones, E., 2015. Global documentation of gullies with the Mars reconnaissance orbiter context camera and implications for their formation. Icarus 252, 236–254. https://doi.org/10.1016/j.icarus.2015.01.022.

Head, J.W., Mustard, J.F., Kreslavsky, M.A., Milliken, R.E., Marchant, D.R., 2003. Recent ice ages on Mars. Nature 426, 797–802. https://doi.org/10.1038/nature02114.

Hecht, M., 2002. Metastability of liquid water on Mars. Icarus 156, 373–386. https://doi.org/10.1006/icar.2001.6794.

Heldmann, J.L., Mellon, M.T., 2004. Observations of martian gullies and constraints on potential formation mechanisms. Icarus 168, 285–304. https://doi.org/10.1016/j.icarus.2003.11.024.

Heldmann, J.L., Carlsson, E., Johansson, H., Mellon, M.T., Toon, O.B., 2007. Observations of martian gullies and constraints on potential formation mechanisms: II. The northern hemisphere. Icarus 188, 324–344. https://doi.org/10.1016/j.icarus.2006.12.010.

Herrick, R.R., Hynek, B.M., 2017. Investigating target versus impactor influences on Martian crater morphology at the simple-complex transition. Meteorit. Planet. Sci. 52, 1722–1743.

Horn, B.K.P., 1981. Hill shading and the reflectance map. Proc. IEEE 69, 14–47. https://doi.org/10.1109/PROC.1981.11918.

Howard, A.D., 2007. Simulating the development of Martian highland landscapes through the interaction of impact cratering, fluvial erosion, and variable hydrologic forcing. Geomorphology 91, 332–363. https://doi.org/10.1016/j.geomorph.2007.04.017, 38th Binghamton Geomorphology Symposium: Complexity in Geomorphology.

Hughes, M.N., Arvidson, R.E., Grant, J.A., Wilson, S.A., Howard, A.D., Golombek, M.P., 2019. Degradation of endeavour crater based on orbital and rover-based observations in combination with landscape evolution modeling. J. Geophys. Res. Plan. 124, 1472–1494. https://doi.org/10.1029/2019JE005949.

Kato, M., Sasaki, S., Takizawa, Y., 2010. The Kaguya mission overview. Space Sci. Rev. 154, 3–19. https://doi.org/10.1007/s11214-010-9678-3.

Kieffer, H.H., Christensen, P.R., Titus, T.N., 2006. CO_2 jets formed by sublimation beneath translucent slab ice in Mars' seasonal south polar ice cap. Nature 442, 793–796. https://doi.org/10.1038/nature04945.

Kneissl, T., Reiss, D., van Gasselt, S., Neukum, G., 2010. Distribution and orientation of northern-hemisphere gullies on Mars from the evaluation of HRSC and MOC-NA data. Earth Planet. Sci. Lett. 294, 357–367. https://doi.org/10.1016/j.

epsl.2009.05.018. Mars Express after 6 Years in Orbit: Mars Geology from Three-Dimensional Mapping by the High Resolution Stereo Camera (HRSC) Experiment.
Kokelaar, B.P., Bahia, R.S., Joy, K.H., Viroulet, S., Gray, J.M.N.T., 2017. Granular avalanches on the moon: mass-wasting conditions, processes, and features. J. Geophys. Res. Plan. 122, 1893–1925. https://doi.org/10.1002/2017JE005320.
Kostama, V.-P., Kreslavsky, M.A., Head, J.W., 2006. Recent high-latitude icy mantle in the northern plains of Mars: characteristics and ages of emplacement. Geophys. Res. Lett. 33 https://doi.org/10.1029/2006GL025946.
Kreslavsky, M.A., Head, J.W., 2000. Kilometer-scale roughness of Mars: results from MOLA data analysis. J. Geophys. Res. Plan. 105, 26695–26711. https://doi.org/10.1029/2000JE001259.
Kumar, P.S., Head, J.W., Kring, D.A., 2010. Erosional modification and gully formation at meteor crater, Arizona: insights into crater degradation processes on Mars. Icarus 208, 608–620. https://doi.org/10.1016/j.icarus.2010.03.032.
Kumar, P.S., Keerthi, V., Kumar, A.S., Mustard, J., Krishna, B.G., Amitabh, Ostrach L.R., Kring, D.A., Kumar, A.S.K., Goswami, J.N., 2013. Gullies and landslides on the moon: evidence for dry-granular flows. J. Geophys. Res. Plan. 118, 206–223. https://doi.org/10.1002/jgre.20043.
Laskar, J., Levrard, B., Mustard, J.F., 2002. Orbital forcing of the martian polar layered deposits. Nature 419, 375–377. https://doi.org/10.1038/nature01066.
Malin, M.C., Edgett, K.S., 2000. Evidence for recent groundwater seepage and surface runoff on Mars. Science 288, 2330–2335. https://doi.org/10.1126/science.288.5475.2330.
Malin, M.C., Bell, J.F., Cantor, B.A., Caplinger, M.A., Calvin, W.M., Clancy, R.T., Edgett, K.S., Edwards, L., Haberle, R.M., James, P.B., Lee, S.W., Ravine, M.A., Thomas, P.C., Wolff, M.J., 2007. Context camera investigation on board the Mars reconnaissance orbiter. J. Geophys. Res. Plan. 112 https://doi.org/10.1029/2006JE002808.
Mangold, N., Mangeney, A., Migeon, V., Ansan, V., Lucas, A., Baratoux, D., Bouchut, F., 2010. Sinuous gullies on Mars: frequency, distribution, and implications for flow properties. J. Geophys. Res. Plan. 115 https://doi.org/10.1029/2009JE003540.
McEwen, A.S., Eliason, E.M., Bergstrom, J.W., Bridges, N.T., Hansen, C.J., Delamere, W. A., Grant, J.A., Gulick, V.C., Herkenhoff, K.E., Keszthelyi, L., Kirk, R.L., Mellon, M.T., Squyres, S.W., Thomas, N., Weitz, C.M., 2007. Mars reconnaissance Orbiter's high resolution imaging science experiment (HiRISE). J. Geophys. Res. Planets. https://doi.org/10.1029/2005JE002605@10.1002/(ISSN)2169-9100.MARSROM1.
Milliken, R.E., Mustard, J.F., Goldsby, D.L., 2003. Viscous flow features on the surface of Mars: observations from high-resolution Mars orbiter camera (MOC) images. J. Geophys. Res. Plan. 108 https://doi.org/10.1029/2002JE002005.
Mischna, M.A., Richardson, M.I., Wilson, R.J., McCleese, D.J., 2003. On the orbital forcing of Martian water and CO2 cycles: a general circulation model study with simplified volatile schemes. J. Geophys. Res. Plan. 108 https://doi.org/10.1029/2003JE002051.
Montgomery, D.R., Korup, O., 2011. Preservation of inner gorges through repeated alpine glaciations. Nat. Geosci. 4, 62–67. https://doi.org/10.1038/ngeo1030.
Perron, J.T., Kirchner, J.W., Dietrich, W.E., 2008. Spectral signatures of characteristic spatial scales and nonfractal structure in landscapes. J. Geophys. Res. Earth Surf. 113 https://doi.org/10.1029/2007JF000866.
Pilorget, C., Forget, F., 2016. Formation of gullies on Mars by debris flows triggered by CO 2 sublimation. Nat. Geosci. 9, 65–69. https://doi.org/10.1038/ngeo2619.
Press, W.H., Teukolsky, S.A., Vetterling, W.T., Flannery, B.P., 1992. Numerical Recipes in C (2nd ed.): The Art of Scientific Computing. Cambridge University Press, USA.
Reiss, D., van Gasselt, S., Neukum, G., Jaumann, R., 2004. Absolute dune ages and implications for the time of formation of gullies in Nirgal Vallis. Mars. J. Geophys. Res. Plan. 109 https://doi.org/10.1029/2004JE002251.
Robbins, S.J., Hynek, B.M., 2012. A new global database of Mars impact craters ≥1 km: 1. Database creation, properties, and parameters. J. Geophys. Res. Plan. 117 https://doi.org/10.1029/2011JE003966.
Robinson, M.S., Brylow, S.M., Tschimmel, M., Humm, D., Lawrence, S.J., Thomas, P.C., Denevi, B.W., Bowman-Cisneros, E., Zerr, J., Ravine, M.A., Caplinger, M.A., Ghaemi, F.T., Schaffner, J.A., Malin, M.C., Mahanti, P., Bartels, A., Anderson, J., Tran, T.N., Eliason, E.M., McEwen, A.S., Turtle, E., Jolliff, B.L., Hiesinger, H., 2010. Lunar reconnaissance orbiter camera (LROC) instrument overview. Space Sci. Rev. https://doi.org/10.1007/s11214-010-9634-2.
Sanders, D., Wischounig, L., Gruber, A., Ostermann, M., 2014. Inner gorge–slot canyon system produced by repeated stream incision (eastern Alps): significance for development of bedrock canyons. Geomorphology 214, 465–484. https://doi.org/10.1016/j.geomorph.2014.03.007.
Schon, S.C., Head, J.W., Fassett, C.I., 2009. Unique chronostratigraphic marker in depositional fan stratigraphy on Mars: evidence for ca. 1.25 Ma gully activity and surficial meltwater origin. Geology 37, 207–210. https://doi.org/10.1130/G25398A.1.
Schorghofer, N., Edgett, K.S., 2006. Seasonal surface frost at low latitudes on Mars. Icarus 180, 321–334. https://doi.org/10.1016/j.icarus.2005.08.022.
Smith, D.E., Zuber, M.T., Frey, H.V., Garvin, J.B., Head, J.W., Muhleman, D.O., Pettengill, G.H., et al., 2001. Mars orbiter laser altimeter: experiment summary after the first year of global mapping of Mars. J. Geophys. Res. 106 (E10), 23689–23722. https://doi.org/10.1029/2000JE001364.
Stopar, J.D., Robinson, M.S., Barnouin, O.S., McEwen, A.S., Speyerer, E.J., Henriksen, M. R., Sutton, S.S., 2017. Relative depths of simple craters and the nature of the lunar regolith. Icarus 298, 34–48. https://doi.org/10.1016/j.icarus.2017.05.022.
Sun, Z., Ulizio, T.P., Fischer, J.N., Levin, J.N., Beer, A.R., Dickson, J.L., Lamb, M.P., 2021. Formation of low-gradient bedrock chutes by dry rockfall on planetary surfaces. Geology. https://doi.org/10.1130/G49286.1 (in press).
Sweeney, J., Warner, N.H., Ganti, V., Golombek, M.P., Lamb, M.P., Fergason, R., Kirk, R., 2018. Degradation of 100-m-scale rocky ejecta craters at the InSight landing site on Mars and implications for surface processes and Erosion rates in the Hesperian and Amazonian. J. Geophys. Res. Plan. 123, 2732–2759. https://doi.org/10.1029/2018JE005618.
Sylvest, M.E., Conway, S.J., Patel, M.R., Dixon, J.C., Barnes, A., 2016. Mass wasting triggered by seasonal CO_2 sublimation under Martian atmospheric conditions: laboratory experiments. Geophys. Res. Lett. 43, 12,363–12,370. https://doi.org/10.1002/2016GL071022.
Tanaka, K.L., Robbins, S.J., Fortezzo, C.M., Skinner Jr., J.A., Hare, T.M., 2014. The digital global geologic map of Mars: chronostratigraphic ages, topographic and crater morphologic characteristics, and updated resurfacing history. Planet. Space Sci. 95, 11–24. https://doi.org/10.1016/j.pss.2013.03.006.
Tesson, P.A., Conway, S.J., Mangold, N., Ciazela, J., Lewis, S.R., Mège, D., 2020. Evidence for thermal-stress-induced rockfalls on Mars impact crater slopes. Icarus 342. https://doi.org/10.1016/j.icarus.2019.113503.
Toon, O.B., Pollack, J.B., Ward, W., Burns, J.A., Bilski, K., 1980. The astronomical theory of climatic change on Mars. Icarus 44, 552–607. https://doi.org/10.1016/0019-1035(80)90130-X.
Watkins, R.N., Jolliff, B.L., Mistick, K., Fogerty, C., Lawrence, S.J., Singer, K.N., Ghent, R. R., 2019. Boulder distributions around young, small lunar impact craters and implications for regolith production rates and landing site safety. JGR Planets 124, 2754–2771. https://doi.org/10.1029/2019JE005963.